University of Groningen

Euclid

 Euclid Collaboration; Camarena, D.; Marra, V.; Sakr, Z.; Nesseris, S.; Da Silva, A.; Garcia-Bellido, J.; Fleury, P.; Lombriser, L.; Martinelli, M.

IMPORTANT NOTE: You are advised to consult the publisher's version (publisher's PDF) if you wish to cite from it. Please check the document version below.

Document Version
Early version, also known as pre-print

[Link to publication in University of Groningen/UMCG research database](#)

Euclid: Testing the Copernican principle with next-generation surveys[⋆]

D. Camarena[1][⋆⋆], V. Marra[2,3,4], Z. Sakr[5,6,7], S. Nesseris[8], A. Da Silva[9,10], J. Garcia-Bellido[8], P. Fleury[11],
L. Lombriser[12], M. Martinelli[13], C. J. A. P. Martins[14,15], J. Mimoso[9,10], D. Sapone[16], C. Clarkson[17], S. Camera[18,19,20],
C. Carbone[21], S. Casas[22], S. Ilić[23,24,5], V. Pettorino[25], I. Tutusaus[12,26,27,5], N. Aghanim[28], B. Altieri[29], A. Amara[30],
N. Auricchio[31], M. Baldi[32,31,33], D. Bonino[20], E. Branchini[34,35], M. Brescia[36], J. Brinchmann[15], G.P. Candini[37],
V. Capobianco[20], J. Carretero[38,39], M. Castellano[13], S. Cavuoti[36,40,41], A. Cimatti[42,43], R. Cledassou[24,44], G. Congedo[45],
L. Conversi[46,29], Y. Copin[47], L. Corcione[20], F. Courbin[48], H. Degaudenzi[49], F. Dubath[49],
C.A.J. Duncan[50,51], X. Dupac[29], S. Dusini[52], A. Ealet[47], S. Farrens[25], P. Fosalba[26,27], M. Frailis[3], E. Franceschi[31],
M. Fumana[21], B. Garilli[21], B. Gillis[45], C. Giocoli[53,54], A. Grazian[55], F. Grupp[56,57], S.V.H. Haugan[58], W. Holmes[59],
F. Hormuth[60], A. Hornstrup[61], K. Jahnke[62], A. Kiessling[59], R. Kohley[29], M. Kunz[12], H. Kurki-Suonio[63], P. B. Lilje[58],
I. Lloro[64], O. Mansutti[3], O. Marggraf[65], F. Marulli[32,31,33], R. Massey[66], M. Meneghetti[67,31], E. Merlin[13], G. Meylan[68],
M. Moresco[32,31], L. Moscardini[32,31,33], E. Munari[3], S.M. Niemi[69], C. Padilla[38], S. Paltani[49], F. Pasian[3], K. Pedersen[70],
G. Polenta[71], M. Poncet[24], L. Popa[72], L. Pozzetti[31], F. Raison[56], R. Rebolo[73,74], J. Rhodes[59], G. Riccio[36],
Hans-Walter Rix[62], E. Rossetti[32], R. Saglia[56,57], B. Sartoris[57,3], A. Secroun[75], G. Seidel[62], C. Sirignano[76,52], G. Sirri[33],
L. Stanco[52], C. Surace[77], P. Tallada-Crespí[78,39], A.N. Taylor[45], I. Tereno[9,79], R. Toledo-Moreo[80], F. Torradeflot[78,39],
E.A. Valentijn[81], L. Valenziano[31,33], Y. Wang[82], G. Zamorani[31], J. Zoubian[75], S. Andreon[83], D. Di Ferdinando[33],
V. Scottez[84,85], M. Tenti[67]

(Affiliations can be found after the references)

October 24, 2022

ABSTRACT

Context. The Copernican principle, the notion that we are not at a special location in the Universe, is one of the cornerstones of modern cosmology. Its violation would invalidate the Friedmann-Lemaître-Robertson-Walker metric, causing a major change in our understanding of the Universe. Thus, it is of fundamental importance to perform observational tests of this principle.
Aims. We determine the precision with which future surveys will be able to test the Copernican principle and their ability to detect any possible violations.
Methods. We forecast constraints on the inhomogeneous Lemaître-Tolman-Bondi (LTB) model with a cosmological constant Λ, basically a cosmological constant Λ and cold dark matter (CDM) model but endowed with a spherical inhomogeneity. We consider combinations of currently available data and simulated *Euclid* data, together with external data products, based on both ΛCDM and ΛLTB fiducial models. These constraints are compared to the expectations from the Copernican principle.
Results. When considering the ΛCDM fiducial model, we find that *Euclid* data, in combination with other current and forthcoming surveys, will improve the constraints on the Copernican principle by about 30%, with ±10% variations depending on the observables and scales considered. On the other hand, when considering a ΛLTB fiducial model, we find that future *Euclid* data, combined with other current and forthcoming datasets, will be able to detect gigaparsec-scale inhomogeneities of contrast −0.1.
Conclusions. Next-generation surveys, such as *Euclid*, will thoroughly test homogeneity at large scales, tightening the constraints on possible violations of the Copernican principle.

Key words. Cosmology: observations – (Cosmology:) cosmological parameters – Space vehicles: instruments – Surveys – Methods: statistical – Methods: data analysis

1. Introduction

Modern cosmology relies on several fundamental assumptions, such as the hypothesis that we do not occupy a special location in the Universe. Thanks to this assumption, called the Copernican principle, cosmologists have made tremendous advances in the understanding of the Universe and laid the foundation of the standard cosmological model. The Copernican principle, along with the fact that the Universe appears to be sta-

tistically isotropic, implies that our Universe is homogeneous and isotropic on sufficiently large scales, eliminating any possible spatial dependence in the cosmological parameters. Equivalently, the space-time is accurately described by the Friedmann-Lemaître-Robertson-Walker (FLRW) metric. Clearly, any violation of the Copernican principle indicates a breakdown of the FLRW paradigm and, therefore, of the standard cosmological model. Thus, testing the Copernican principle is an essential task in cosmology.

One of the most fundamental tests of the Copernican principle comes from observations of our motion with respect to

---

the cosmic microwave background (CMB) rest frame, which induces a kinematic dipole that has already been observed in the CMB (Aghanim et al. 2014; Akrami et al. 2020; Ferreira & Quartin 2021; Saha et al. 2021), the local bulk flow (Colin et al. 2011; Feindt et al. 2013; Hudson et al. 2004; Carrick et al. 2015), X-ray clusters (Migkas et al. 2020, 2021), type Ia supernovae (SNe; Mohayaee et al. 2021; Rahman et al. 2022), high redshift radio sources (Colin et al. 2017; Bengaly et al. 2018; Siewert et al. 2021), and distant quasars (Secrest et al. 2021).[1] Many of these observations have intrinsic systematic errors that have to be taken into account (Dalang & Bonvin 2022) in order to avoid theoretical biases. Another route is to perform null tests of the FLRW metric (see Nesseris et al. 2022, for recent forecasts) or to estimate the homogeneity scale (Yadav et al. 2010; Kim et al. 2022).

Additionally, it is also possible to test the Copernican principle by assuming an inhomogeneous metric, such as that of the Lemaître-Tolman-Bondi (LTB) model (Garcia-Bellido & Haugboelle 2008a; February et al. 2010; Valkenburg et al. 2014; Redlich et al. 2014). In fact, current observations can meaningfully test the Copernican principle, leading to constraints on deviations from the FLRW metric at almost the cosmic variance level (Camarena et al. 2021).

In this paper we explore the precision with which next-generation surveys will probe for violations of the Copernican principle. Specifically, we focus on *Euclid* (Laureijs et al. 2011), which is an M-class space mission of the European Space Agency planned to be launched in 2023. The satellite will carry two instruments on board – the visible imager (VIS; Cropper et al. 2018) and the near-infrared spectrophotometric instrument (Prieto et al. 2012; Maciaszek et al. 2016) – which will carry out a photometric and spectroscopic galaxy survey covering over $15\,000\,\mathrm{deg}^2$ of the sky, with the aim of measuring the growth of the large-scale structure (LSS) up to a redshift of $z \sim 2$ (Euclid Collaboration et al. 2022).

Euclid will have two main, complementary cosmological probes, namely galaxy clustering and weak lensing from the photometric survey and galaxy clustering from the spectroscopic survey. While photometric surveys image a larger number of galaxies than spectroscopic ones, they also have larger redshift uncertainties. On the other hand, spectroscopic galaxy surveys have much higher radial precision, but target many fewer objects. *Euclid* has very high spectroscopic accuracy; it will be able to make very precise measurements of galaxy clustering that also include the radial dimension, that is to say, it will be able to probe clustering along the line of sight. In this work we create mock baryon acoustic oscillation (BAO) data, in accordance with *Euclid*'s spectroscopic survey specifications, based on the Fisher matrix approach of Euclid Collaboration: Blanchard et al. (2020, hereafter EC20)

Furthermore, we also stress some of the possible synergies between *Euclid* and other contemporary surveys. The latter include the Legacy Survey of Space and Time (LSST) performed at the *Vera C. Rubin* Observatory (Abell et al. 2009) and that of the Dark Energy Spectroscopic Instrument (DESI; Aghamousa et al. 2016) since they will be complementary to *Euclid* in terms of redshift, thus significantly extending the possible redshift range of our analysis.

Finally, forecast constraints on deviations from the Copernican principle were presented in Amendola et al. (2018), where a joint analysis between *Euclid* (Laureijs et al. 2011) and a stage

IV SN mission (Albrecht et al. 2006, assuming SNAP as a concrete example) was performed. Here we update the constraints of this analysis by using more recent *Euclid* specifications (see EC20) while also considering synergies with other surveys.

This paper is organised as follows: In Sect. 2 we briefly review the dynamics of a spherically inhomogeneous space-time based on the LTB metric but with the addition of a cosmological constant, Λ (i.e. the ΛLTB model) and discuss our particular choices for its arbitrary functions. In Sect. 3 we present the data used in our analysis and explain how mock catalogues are produced considering particular fiducial cosmologies, while in Sect. 4 we define and discuss the Copernican prior. Our results are presented and discussed in Sect. 5 and Sect. 6. We conclude in Sect. 7.

2. Spherically symmetric inhomogeneous models with a cosmological constant

A spherically inhomogeneous space-time can be modelled using the ΛLTB model, which practically is a standard cosmological constant Λ and cold dark matter (CDM) model endowed with a spherical inhomogeneity. Here, we aim to test the homogeneity of the Universe, and thus, we neglect anisotropic degrees of freedom by placing the observer at the centre of the spherical inhomogeneity. In this section we briefly review the ΛLTB model presented in Camarena et al. (2021);[2] a comprehensive review is given in Marra et al. (2022).

Hereafter, we use a prime to denote a partial derivative with respect to the radial coordinate, r, while we use a dot to denote a partial derivative with respect to the time coordinate, t.

2.1. Dynamics

The LTB metric can be written as

$$\mathrm{d}s^2 = -c^2\mathrm{d}t^2 + \frac{R'^2(t,r)}{1 - K(r)\,r^2}\mathrm{d}r^2 + R^2(r,t)\left(\mathrm{d}\theta^2 + \sin^2\theta\,\mathrm{d}\phi^2\right), \quad (1)$$

where the curvature $K(r)$ is an arbitrary function of the radial coordinate. The FLRW metric can be recovered by imposing $K = $ constant and $R = a(t)\,r$, with $a(t)$ as the FLRW scale factor. From the line element Eq. (1), we can define the transverse and longitudinal scale factors, $a_\perp = R(r,t)/r$ and $a_\parallel = R'(r,t)$, respectively. The two scale factors define two different expansion rates given by

$$H_\perp(t,r) \equiv \frac{\dot{a}_\perp}{a_\perp}, \qquad H_\parallel(t,r) \equiv \frac{\dot{a}_\parallel}{a_\parallel}. \quad (2)$$

Solving Einstein's equations with a cosmological constant, we obtain an equation analogue to the first Friedmann equation,

$$\frac{H_\perp^2}{H_{\perp 0}^2} = \Omega_{\mathrm{m},0}\left(\frac{a_{\perp 0}}{a_\perp}\right)^3 + \Omega_{k,0}\left(\frac{a_{\perp 0}}{a_\perp}\right)^2 + \Omega_{\Lambda,0}, \quad (3)$$

where the present-day density parameters are now functions of r,

$$\Omega_{\Lambda,0}(r) = \frac{\Lambda c^2}{3 H_{\perp 0}^2}, \quad (4)$$

$$\Omega_{k,0}(r) = -\frac{K(r)\,c^2}{H_{\perp 0}^2\,a_{\perp 0}^2}, \quad (5)$$

$$\Omega_{\mathrm{m},0}(r) = \frac{2\,m(r)}{H_{\perp 0}^2\,a_{\perp 0}^3\,r^3}, \quad (6)$$

---

[1] See also (Aluri et al. 2022), and references therein, for a recent review of observational tests of the FLRW paradigm.

[2] The notation adopted here differs from the notation used in Camarena et al. (2021).

which satisfy $\Omega_{m,0}(r) + \Omega_{k,0}(r) + \Omega_{\Lambda,0}(r) = 1$. It should be noted that we have defined $H_{\perp 0} \equiv H_\perp(t_0, r)$ and $a_{\perp 0} \equiv a_\perp(t_0, r)$.

From Eq. (6) we can see that Einstein's equations introduce another arbitrary function: the Euclidean mass $m(r)$. This function arises as a constant of integration and is defined via

$$m(r) = \int_0^r \mathrm{d}r' \, 4\pi G \, \rho_m(t, r') \, a_\parallel a_\perp^2 r'^2 \,, \tag{7}$$

where $\rho_m(t, r)$ is the local matter density.

Another arbitrary function of the ΛLTB model is the Big Bang function, $t_{BB}(r)$. This can be interpreted as the time corresponding to the Big Bang singularity surface, and it emerges from integration of Eq. (3):

$$t - t_{BB}(r) = \frac{1}{H_{\perp 0}(r)} \int_0^\chi \frac{\mathrm{d}x}{\sqrt{\Omega_{m,0}(r)x^{-1} + \Omega_{k,0}(r) + \Omega_{\Lambda,0}(r)x^2}} \,, \tag{8}$$

where $\chi = a_\perp(t, r)/a_{\perp 0}$. We note that the last integral defines the age of the Universe, t_0, when integrated from zero to one.

Finally, from the line element Eq. (1) it follows that the geodesic equations are

$$\frac{\mathrm{d}t}{\mathrm{d}z} = -\frac{1}{(1 + z) H_\parallel(t, r)} \,, \qquad \frac{\mathrm{d}r}{\mathrm{d}z} = -\frac{c \sqrt{1 - K(r)r^2}}{(1 + z) a_\parallel(t, r) H_\parallel(t, r)} \,. \tag{9}$$

2.2. Free functions

As shown above, the ΛLTB model has three arbitrary functions: $K(r)$, $m(r)$, and $t_{BB}(r)$. One of these functions is just a gauge freedom that can be fixed by re-scaling the radial coordinate. Here, we fix the radial coordinate r such that the mass function satisfies $m(r) \propto r^3$; we will later present the missing normalisation of the Euclidean mass. On the other hand, a Big Bang function different from zero introduces decaying modes into the matter density (Silk 1977). The presence of these modes leads to a disagreement with the standard scenario of inflation (Zibin 2008). Thus, to ensure the absence of decaying modes on the matter density we set $t_{BB}(r) = 0$, which also implies that the Big Bang singularity happens everywhere simultaneously.

Hence, we end up with just one arbitrary function, the curvature profile $K(r)$. Here, we adopt the monotonic compensated profile given by

$$K(r) = K_B + (K_C - K_B) P_3(r/r_B) \,, \tag{10}$$

where r_B is the comoving radius of the spherical inhomogeneity, K_B is the background curvature, K_C is the central curvature, and the function P_3 follows,

$$P_3(x) = \begin{cases} 1 - \exp\left[-(1-x)^3/x\right] & \text{for } 0 \le x < 1 \\ 0 & \text{for } 1 \le x \end{cases}, \tag{11}$$

with $x = r/r_B$. Thus, Eq. (10) ensures a smooth transition between the LTB and FLRW metrics; the ΛLTB model asymptotes to the ΛCDM model at scales $r \ge r_B$.

We note that while we have fixed $m(r)$ and $t_{BB}(r)$ using physical arguments, our choice of $K(r)$ remains arbitrary and could have a significant impact on our analysis. In Appendix A we discuss our choice and compare it with another ΛLTB model. We also present an extra analysis performed using an extension of Eq. (10). This further analysis shows that a more generalised curvature profile could weaken the constraints by up to a factor of ~ 2.

Once the three arbitrary functions are fixed, we can compute $\rho_m(r, t)$ in order to determine the matter density contrast using

$$\delta(r, t) := \frac{\rho_m(r, t)}{\rho_m(r_B, t)} - 1 \,, \tag{12}$$

and we can also compute the mass (integrated) density contrast via

$$\Delta(r, t_0) = \frac{4\pi \int_0^r \mathrm{d}\bar{r} \, \delta(\bar{r}, t_0) \, a_\perp^2(\bar{r}, t_0) a_\parallel(\bar{r}, t_0) r^2}{4\pi \, a_\perp^3(r, t_0) \, r^3/3} \tag{13}$$

$$= \frac{m(r)}{4\pi G \, R^3(r, t_0)/3 \, \rho_m^{out}(t_0)} - 1 = \frac{\Omega_{m,0}(r)}{\Omega_{m,0}^{out}} \left[\frac{H_{\perp 0}(r)}{H_{\perp 0}^{out}}\right]^2 - 1 \,.$$

Here we use the superscript 'out' to denote the FLRW background quantities outside the inhomogeneity, for example $\rho_m(r_B, t_0) = \rho_m^{out}(t_0)$. We additionally make use of the FLRW comoving coordinate at the present time, which is defined as

$$r^{out} := r \, a_{\perp 0}(r)/a^{out}(t_0) \,. \tag{14}$$

The top panel in Fig. 1 shows the matter and integrated mass density contrast as a function of r^{out} at $t = t_0$ for a deep and gigaparsec-scale void. Also displayed in the figure are $\Omega_{m,0}(r^{out}) - \Omega_{m,0}^{out}$ and $\Omega_{k,0}(r^{out}) - \Omega_{k,0}^{out}$, giving the deviations of the matter and curvature densities with respect to their ΛCDM counterparts (middle panel), along with the deviations of the transverse and longitudinal expansion rates with respect to H_0^{out} (bottom panel).

It is important to highlight that the assumption of the profile Eq. (10) implicitly introduces a compensating scale, here denoted by $r_L^{out}[\delta(r_L^{out}, t) = 0]$, at which the central overdense or underdense region makes a transition to the surrounding mass-compensating underdense or overdense region. The r_L^{out} and the r_B^{out} scales are represented in Fig. 1 by the dotted vertical lines. Furthermore, one can note that at the centre of the inhomogeneity $\Delta(0, t) = \delta(0, t)$, while at the boundary shell we have $\Delta(r_B, t) = \delta(r_B, t) = 0$. Since the LTB and FLRW metrics perfectly match at the boundary shell, then we have that $r_B^{out} = r_B$. Finally, from Eq. (6) is possible to determine the missing normalisation of the Euclidean mass; specifically we find $m(r) = \Omega_{m,0}^{out} (H_0^{out})^2 r^3/2$, while Eq. (5) leads to $K_B = -\Omega_{k,0}^{out} (H_0^{out})^2$.

2.3. Parameter space

We used the `monteLLTB` code to solve the dynamical equations and then to sample the parameter space of the ΛLTB model.[3] The `monteLLTB` code combines `montepython` (Audren et al. 2013; Brinckmann & Lesgourgues 2019) for the Markov chain Monte Carlo parameter space exploration and likelihoods, `class` (Blas et al. 2011) for the CMB computation and `voiddistances2020` (Valkenburg 2012) for the ΛLTB metric functions via a wrapper that translates the `montepython` trial vector into an effective FLRW vector that is suitable for `class` (see Camarena et al. 2021 for details).

Since the LTB metric asymptotes to FLRW at $r \ge r_B$, the background expansion of our model is specified by the standard six ΛCDM parameters: the normalised Hubble constant $h := H_0/100$, the baryon density $\Omega_{b,0}$, the cold dark matter density $\Omega_{cdm,0}$, the optical depth τ, the amplitude of the power spectrum A_s and its tilt n_s.

On the other hand, the spherically inhomogeneous region is fixed by the boundary redshift, z_B, and the mass density contrast
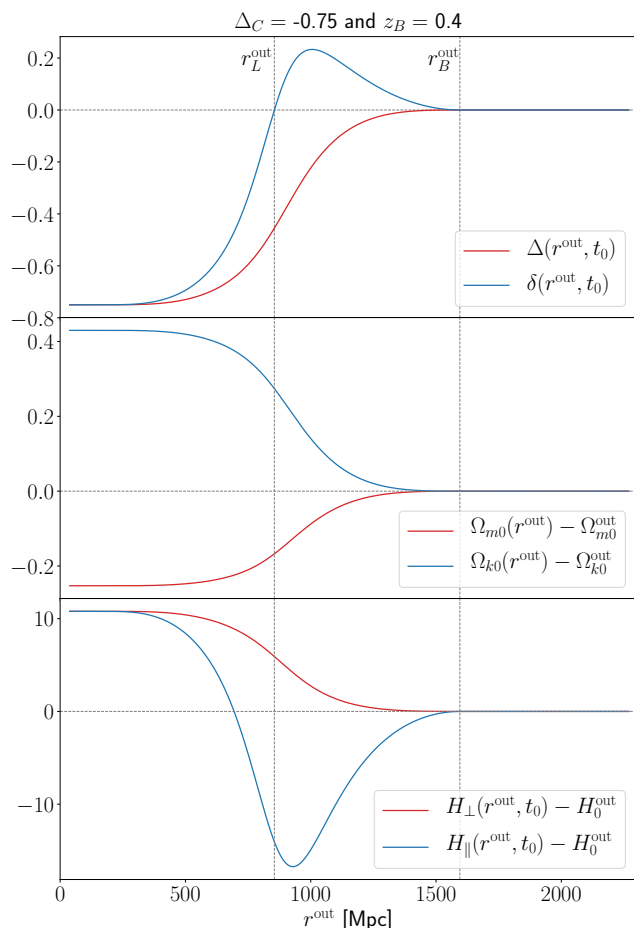
---

[3] https://github.com/davidcato/monteLLTB

Fig. 1. Several ΛLTB quantities as a function of the FLRW comoving coordinate r^{out}. Top: Density contrast of matter, $\delta(r) = \rho_{\text{m}}(r, t_0)/\rho_{\text{m}}(r_{\text{B}}, t_0) - 1$, and integrated mass, $\Delta(r)$, as functions of the FLRW comoving coordinate. At radius $r_{\text{L}}^{\text{out}}$ the central structure ends and the compensating shell begins, while $r_{\text{B}}^{\text{out}}$ is the boundary of the spherical inhomogeneity. Middle: Deviations from the background density of matter, $\Omega_{\text{m,0}}^{\text{out}}$, and curvature, $\Omega_{k,0}^{\text{out}}$, as a function of the FLRW comoving coordinate due to the radial dependence on $\Omega_{\text{m,0}}(r)$ and $\Omega_{k,0}(r)$. We note that the FLRW background quantities are recovered for $r \geq r_{\text{B}}^{\text{out}}$. Bottom: Transverse and longitudinal fluctuations in the expansion rates as a function of the FLRW comoving coordinate.

at the centre of the inhomogeneity, $\Delta_{\text{C}} \equiv \Delta(0, t)$. The parameters z_{B} and Δ_{C} are related to the parameters r_{B} and K_{C}, which explicitly appear in the definition of the curvature profile. As discussed in Sect. 4, we conveniently present our results using the compensating scale $r_{\text{L}}^{\text{out}}$ and the mass contrast at such a scale, $\Delta_{\text{L}} \equiv \Delta(r_{\text{L}}, t_0)$.

We note that for $\Delta_{\text{C}} \approx 0$, the parameter space is highly degenerate so that the model could feature arbitrarily large values of z_{B} and be still allowed by the data. In order to overcome this issue, we adopt, as in Camarena et al. (2021), the flat prior $z_{\text{B}} \in [0, 0.5]$. This prior allows us to map non-Copernican structures of up to $r_{\text{L}}^{\text{out}} \sim 1$ Gpc.

3. Data

Here we present both the forecast and current data used to constrain the ΛLTB model. Although our goal is to forecast constraints on the Copernican principle given the forthcoming surveys, the inclusion of current data is needed to tightly constrain the ΛLTB parameter space at small scales.

Table 1. Parameter values for the fiducial models that are used for the mocks. The values used for the ΛCDM follow the fiducial of EC20; in particular, spatial flatness is assumed. The Hubble constant H_0 is shown in units of km s^{-1} Mpc^{-1}, while the absolute magnitude of the SN M_0 is shown in units of mag.

model	M_0	$\Omega_{\text{m,0}}$	$\Omega_{\text{b,0}}h^2$	H_0	Δ_{C}	z_{B}
ΛCDM	-19.3	0.32	0.02225	67	-	-
ΛLTB 1	-19.3	0.32	0.02225	67	-0.5	0.05
ΛLTB 2	-19.3	0.32	0.02225	67	-0.1	0.4
ΛLTB 3	-19.3	0.32	0.02225	67	-0.1	0.8

Forecasted datasets are generated considering four fiducial models, which are based on the ΛCDM and ΛLTB models (see Table 1). By considering the ΛCDM forecast data we aim to determine the precision with which next-generation surveys will be able to probe for deviations from the FLRW metric. Meanwhile, by considering the inhomogeneous ΛLTB fiducial model, we aim to investigate the ability of future surveys to detect a violation of the Copernican principle. In order to assume a consistent fiducial model, current data have been re-scaled to agree with the aforementioned fiducial models. Such a re-scaling is performed following the procedure described in Appendix B. Furthermore, we also assume that there are no tensions among the different datasets; this includes tensions between early and late determinations. The theoretical predictions for the observables implemented here follow the equations discussed in Sect. 3 of Camarena et al. (2021). We note that, in order to fully calibrate the SN distances, we also assume a fiducial value for the absolute magnitude of SN data, that is, $M_0 = -19.3$.

3.1. Forecast data

In order to forecast how *Euclid* and other forthcoming surveys will constrain deviations from the Copernican principle, we created mock SN and BAO data; the former provide information on the luminosity distance, while the latter concern the Hubble parameter and the angular diameter distance. In particular, the recipes described here were used for the ΛCDM catalogues, while the ΛLTB catalogues are obtained by suitably re-scaling the former (see Appendix B).

The four fiducial cosmologies based on the ΛCDM and the ΛLTB model that we consider here are shown in Table 1; the former was also used in EC20. To make the mocks for the ΛCDM model, we calculated the redshift evolution of the Hubble parameter, along with the luminosity and angular diameter distances, using the recipe described in the next section, which is based on the specifications of *Euclid* and other LSS surveys. On the other hand, as mentioned before, the ΛLTB mock catalogues are obtained following the process described in Appendix B. Since computing correlation matrices for models far from the ΛCDM model is currently not possible (Harnois-Deraps et al. 2019; Friedrich et al. 2021; Ferreira & Marra 2022), we first compute the correlation matrix assuming the ΛCDM model. Then, we apply the method described in Appendix B to obtain the corresponding ΛLTB matrices.

Since future surveys like *Euclid* are expected to provide observations with high precision, it is important to be convinced that our analysis methods will be robust. Hence, in order to un-

derstand and take possible observational systematic uncertainties that can affect the measurements into account, several analyses, such as that of Euclid Collaboration: Paykari et al. (2020), have been performed. In the latter, the observational systematic effects of the *Euclid* VIS instrument were studied, taking the modelling of the point spread function and the charge transfer inefficiency into account. Since these systematic effects are expected to be better understood by the time the data arrive, in this analysis we assume that they will be under control in the final data products. In any case, in what follows we in fact include several astrophysical systematic effects, such as the galaxy bias, as discussed in what follows.

3.1.1. SN surveys

In our analysis we focus on two forthcoming SN surveys, the first of which is based on the proposed *Euclid* DESIRE survey (Laureijs et al. 2011; Astier et al. 2014), while the second one is based on the specifications of the LSST. In particular, we assume that the *Euclid* DESIRE survey will observe 1700 SNe in the redshift range $z \in [0.7, 1.6]$, while the one from the LSST survey will observe 8800 SNe in the redshift range $z \in [0.1, 1.0]$, thus resulting in a total of 10 500 points.

In either case we consider the redshift distributions of the SN events as described in Astier et al. (2014), assuming the points are not correlated with each other. Even though the *Euclid* SN survey is not currently guaranteed to take place, we decided to include it in order to extend the redshift range of LSST at high z. For the SN mocks we include an observational error of the form $\sigma_{\mathrm{tot},i}^2 = \delta\mu_i^2 + \sigma_{\mathrm{flux}}^2 + \sigma_{\mathrm{scat}}^2 + \sigma_{\mathrm{intr}}^2$, where the terms corresponding to the intrinsic contributions, the scatter and the flux are the same for all events: $\sigma_{\mathrm{intr}} = 0.12$, $\sigma_{\mathrm{scat}} = 0.025$, and $\sigma_{\mathrm{flux}} = 0.01$, respectively. Finally, we also include an error on the distance modulus $\mu = m - M_0$ that scales linearly with z as $\delta\mu = e_{\mathrm{M}} z$, where e_{M} follows a Gaussian distribution with zero mean and standard deviation $\sigma(e_{\mathrm{M}}) = 0.01$ (see Gong et al. 2010; Astier et al. 2014), which includes the possible redshift evolution of SNe not taken into account by the distance estimator (see Astier et al. 2014). However, while a value of $e_{\mathrm{M}} = 0.01$ is required to take a possible systematic evolution into account, this would be added quadratically to an effective term of $e_{\mathrm{M}} = 0.055$ arising from SN lensing. The latter has been theoretically calculated by several authors to be of the order of $\sigma_{\mathrm{lens}} \simeq 0.055 z$, for example $\sigma_{\mathrm{lens}} = 0.052 z$ (Marra et al. 2013; Quartin et al. 2014), and $\sigma_{\mathrm{lens}} = 0.056 z$ (Ben-Dayan et al. 2013), while observationally it was determined, via the Supernova Legacy Survey to be $\sigma_{\mathrm{lens}} = (0.055 \pm 0.04) z$ (Jonsson et al. 2010) and $\sigma_{\mathrm{lens}} = (0.054 \pm 0.024) z$ (Kronborg et al. 2010).

3.1.2. Local prior on the Hubble constant

We also forecast a 1% measurement of the Hubble constant, which is the grand goal of the SH0ES collaboration,

$$H_0 = \begin{cases} 67.00 \pm 0.67 \, \mathrm{km \, s^{-1} \, Mpc^{-1}} & \text{for } \Lambda\mathrm{CDM} \\ 67.62 \pm 0.68 \, \mathrm{km \, s^{-1} \, Mpc^{-1}} & \text{for } \Lambda\mathrm{LTB} \, 1 \\ 68.22 \pm 0.68 \, \mathrm{km \, s^{-1} \, Mpc^{-1}} & \text{for } \Lambda\mathrm{LTB} \, 2 \\ 68.45 \pm 0.68 \, \mathrm{km \, s^{-1} \, Mpc^{-1}} & \text{for } \Lambda\mathrm{LTB} \, 3 \end{cases}, \quad (15)$$

where the central value is given by the fiducial H_0 value for the ΛCDM fiducial model, meanwhile for the ΛLTB models this central value is the expected value given the methodology described in Appendix C. Here, as mentioned earlier, we consider the

a scenario in which there is no tension between early and late determinations of the Hubble constant. By assuming a single consistent fiducial model, we focus on the constraining potential of future surveys to test the Copernican principle, leaving the issue of the Hubble tension to other studies. This is in part justified since Camarena et al. (2021, 2022) shown that a large inhomogeneity cannot explain away the Hubble tension. Finally, we impose the Gaussian prior of Eq. (15) on H_0^{L}; the corresponding Hubble constant value for an inhomogeneous model (see Appendix C for a detailed discussion).

3.1.3. Large-scale structure surveys

Here, we now briefly describe our procedure for creating mock BAO data based on the specifications of *Euclid* via a Fisher matrix approach, following the methodology of EC20 for the spectroscopic survey, on which we focus since we are interested in obtaining precise measurements of the angular diameter distance $D_{\mathrm{A}}(z)$ and the Hubble parameter $H(z)$. We do not consider weak lensing by *Euclid*, nor other perturbation level observables such as redshift space distortions, because there is not yet a fully developed linear perturbation theory on inhomogeneous backgrounds such as the LTB. [4] A discussion and the numerical simulation of the LSS on an LTB background is provided in Marra et al. (2022) and references therein.

As was extensively discussed in EC20, the main targets of the Euclid survey will be emission line galaxies (ELGs), which are bright emitters in specific lines, such as H_α and [O III], that can be seen in the redshift range $z \in [0.9, 1.8]$, and can be used to measure the galaxy power spectrum. In particular, *Euclid* will determine approximately 30 million spectroscopic redshifts with an uncertainty of $\sigma_z = 0.001(1 + z)$ (Pozzetti et al. 2016), which will provide the galaxy power spectrum with information on the distortions due to the redshift uncertainty, the residual shot noise, the Alcock-Paczynski effect, the redshift space distortions and the galaxy bias. Furthermore, non-linear effects, such as a non-linear smearing of the BAO feature or a non-linear scale-dependent galaxy bias that distorts the shape of the power spectrum, have also been taken into account (see Wang et al. 2013 and de la Torre & Guzzo 2012, respectively).

In this work we again make use of the same binning scheme as in Martinelli et al. (2020, 2021), which differs from that of EC20. In particular, instead of four equally spaced redshift bins, we now consider nine bins of width $\Delta z = 0.1$. After re-binning the data provided in EC20, we obtain the following specifications for the galaxy number density $n(z)$, given in units of $\mathrm{Mpc^{-3}}$, and that of the galaxy bias $b(z)$:

$$n(z) = \{2.04, 2.08, 1.78, 1.58, 1.39, 1.15, 0.97, 0.7, 0.6\} \times 10^{-4}, \quad (16)$$
$$b(z) = \{1.42, 1.5, 1.57, 1.64, 1.71, 1.78, 1.84, 1.90, 1.96\}. \quad (17)$$

In Martinelli et al. (2020) we tested our choice for the binning scheme against that of EC20, and we found the results were in agreement.

In the case of the ΛCDM mocks, the Fisher matrix for the cosmological parameters, along with the associated covariance matrix, can be derived by following the methodology described in EC20. The cosmological parameters we consider for the ΛCDM mocks include the background quantities $\{\omega_{\mathrm{m}} = \Omega_{\mathrm{m},0}h^2, h, \omega_{\mathrm{b}} = \Omega_{\mathrm{b},0}h^2, n_{\mathrm{s}}\}$, two non-linear parameters $\{\sigma_{\mathrm{p}}, \sigma_{\mathrm{v}}\}$ (see EC20) and the five redshift-dependent parameters

---

[4] See, however, Moss et al. (2011); Ishak et al. (2013) for a comparison with observations.

{$\ln D_\text{A}$, $\ln H$, $\ln f\sigma_8$, $\ln b\sigma_8$, P_s}, which are estimated in every redshift bin. Here we have defined $f\sigma_8 \equiv f(z)\sigma_8(z)$ as the linear growth rate multiplied by σ_8, which corresponds to the RMS fluctuations in the matter mass density in a comoving sphere of $8\,h^{-1}$ Mpc, while $b\sigma_8 \equiv b(z)\sigma_8(z)$ and P_s are the galaxy bias and the shot noise, respectively (see EC20). From this we can then estimate the expected uncertainty of the measurements of the *Euclid* survey for both the angular diameter distance $D_\text{A}(z)$ and the Hubble parameter $H(z)$, in every redshift bin, while all other parameters are marginalised over. Furthermore, we apply the approach presented in Appendix B to obtain the corresponding ΛLTB mock data.

Since the spectroscopic survey of *Euclid* will only cover the redshift range $z \in [0.9, 1.8]$, this limits the range where SN and BAO data will be obtained. Hence, in order to cover smaller redshifts we complement our analysis by using fiducial data products from the DESI survey as well. DESI has already initiated survey operations in 2021 and will eventually obtain spectra for tens of millions of galaxies and quasars up to $z \sim 4$, thus making redshift-space distortion and BAO analyses possible. To create DESI mocks, assuming the ΛCDM model, we follow the methodology for both the angular diameter distance $D_\text{A}(z)$ and the Hubble parameter $H(z)$, as described in Aghamousa et al. (2016). These Fisher matrix forecasts were also derived using the full anisotropic galaxy power spectrum (i.e. measurements of the matter power spectrum as a function of the angle with respect to the line of sight), as described in Font-Ribera et al. (2014). This approach is similar to that of the *Euclid* forecasts and it also includes all information from the two-point correlation function. In particular, the baseline DESI survey will cover approximately $14\,000\,\text{deg}^2$ and will target ELGs, luminous red galaxies, bright galaxies, and quasars, all in the redshift range $z \in [0.05, 3.55]$, although the precision of the measurements will depend on the target population. Regarding the specific populations, the bright galaxies will be in the range $z \in [0.05, 0.45]$ in five equally spaced redshift bins, while the ELGs and the luminous red galaxies will be in the range $z \in [0.65, 1.85]$ in 13 equally spaced bins. Finally, the Ly-α forest quasars will be in the range $z \in [1.96, 3.55]$ in 11 equally spaced bins and we assume that the points are uncorrelated with each other.

In the case when we used the combination of *Euclid* and DESI data together, in order to avoid overlap between the two surveys at late times, we only considered the DESI points that do not overlap with those of *Euclid*, because an overlap will lead to undesired correlations between the surveys. Moreover, since the DESIRE + LSST SN points will only reach at most $z = 1.6$, we included the DESI data up to $z = 0.9$, thus omitting the Ly-α forest observations. However, when used separately we considered the full redshift range of the datasets.

3.2. Current data

As shown in Camarena et al. (2021), CMB and SN data are necessary in order to obtain tight constraints on the ΛLTB model. For our particular case, this means that the presence of real data (i.e. *Planck* 2018 and Pantheon SNe) is needed even though our analysis aims to forecast the contribution of forthcoming surveys. The inclusion of CMB data is crucial to constrain the background parameters, while the usage of low-z SNe allows us to break the degeneracy of the ΛLTB parameters model at small scales. As discussed at the beginning of the present Sect., we rescale current data according to the predictions of the fiducial models shown in Table 1 and following the procedure described in Appendix B.

3.2.1. Cosmic microwave background

When the ΛCDM forecast data are considered, we perform our analysis including the latest *Planck* CMB data[5] (Aghanim et al. 2020b). We use the high-ℓ TT+TE+EE, low-ℓ TT, and low-ℓ EE likelihoods. Particularly, we use the compressed version of high-ℓ data, that is, the likelihood normalised over all nuisance parameters except A_planck. We note that typical constraints obtained for ΛCDM using these likelihoods include the fiducial values adopted for the forecast data (Table 1) within 68% uncertainties, allowing the combination of CMB and forecast data without the necessity of applying the re-scaling technique.

On the other hand, the ΛLTB cosmologies presented on Table 1 could significantly change the CMB power spectra and lead to disagreements of these with the constraints of the aforementioned likelihoods. Thus, one should change the *Planck* CMB data according to the ΛLTB fiducial cosmologies. This is not a trivial task given the complex structure of the CMB likelihoods and our limited understanding of perturbations on the inhomogeneous models. Thus, for our analyses of the ΛLTB mock data we use the CMB distance priors on the shift parameter R, the acoustic scale l_A, the amount of baryons $\Omega_\text{b}h^2$, and the tilt of the power spectrum n_s. We build the mock CMB priors considering the current measurements given by Chen et al. (2019).

3.2.2. SN surveys

The lack of SN data at very low redshifts $z \sim 0.01$ – the lowest LSST point lies at $z = 0.1$ – increases the degeneracy between Δ_C and z_B, loosening the constraints on the ΛLTB model. To overcome this issue, we include the Pantheon SN compilation (Scolnic et al. 2018).

3.2.3. Large-scale structure surveys

We also include BAO data from 6dFGS (Beutler et al. 2011), SDSS-MGS (Ross et al. 2015) and BOSS-DR12 (Alam et al. 2017) surveys. The isotropic measurements from 6dFGS and SDSS-MGS allow us to access redshifts 0.1 and 0.15, respectively, while BOSS provides anisotropic measurements at redshifts 0.38, 0.51, and 0.61. We note that these current data overlap with our forecast DESI catalogues, but we assume no correlations between these datasets. Hereafter we collectively refer to this set of data as BAOs. We note that our analysis does not include the latest eBOSS data (Ross et al. 2020; Raichoor et al. 2020; Lyke et al. 2020; du Mas des Bourboux et al. 2020) chiefly because the eBOSS dataset spans over all the redshift range of our forecast *Euclid* data.

3.2.4. y-Compton distortion and the kSZ effect

Finally, when forecast data from ΛCDM were analysed, we introduced priors on the y-Compton distortion and the kinetic Sunyaev-Zeldovich (kSZ) effect. For the y-Compton distortion, we adopted the upper limit prior at 95.4% uncertainty provided by COBE-FIRAS $y < 1.5 \times 10^{-5}$ (Fixsen et al. 1996). Meanwhile, for the kSZ effect we adopted the $\sim 47\%$ constraint from SPT-SZ and SPTpol surveys (Reichardt et al. 2021). Considering the ΛCDM fiducial, we implemented the Gaussian prior on the kSZ amplitude as $D_{3000} = (3.49 \pm 1.63)\,\mu\text{K}$.

Priors on the y-Compton distortion and the kSZ effect were not used for our analysis of the ΛLTB forecast data since they do

---

[5] http://www.esa.int/Planck

not improve upon constraints given by the combinations of the other datasets.

4. Copernican prior

In the absence of the Copernican principle, the LSS of the Universe may feature arbitrary radial inhomogeneities. In an FLRW model, instead, those structures are constrained by the Copernican principle. Such constraints can be obtained through linear perturbation theory. Assuming that the density contrast $\Delta(r)$ is a Gaussian field, we can compute its RMS by

$$\sigma^2(r) = \int_0^\infty \frac{dk}{k} \left[\frac{k^3 P_{m,0}(k)}{2\pi} \frac{3 j_1(rk)}{rk} \right]^2 , \qquad (18)$$

where $P_{m,0}(k)$ is the standard power spectrum today and j_1 is the spherical Bessel function of the first kind. The aforementioned quantities can be used to define a prior that establishes the probability of finding an inhomogeneous deviation from the FLRW at a given scale. Such a prior is the so-called Copernican prior and can be used to constrain Δ_C and z_B through (Camarena et al. 2021)

$$\mathcal{P}(\Delta_C, z_B) \propto \exp\left[-\frac{1}{2} \frac{\Delta^2(r_L, t_0)}{\sigma^2(r_L^{out})} \right], \qquad (19)$$

where $\Delta(r, t_0)$ is given by Eq. (13), $r_L(\Delta_C, z_B)$ is the radius of the central under/overdensity, and $r_L^{out}(\Delta_C, z_B)$ is the latter radius in the FLRW comoving coordinates of Eq. (14). We note that $r_L^{out}(\Delta_C, z_B)$ is the scale of interest since it defines the size of the central under/overdensity. Additionally, by definition the Copernican prior vanishes at the matching shell, r_B^{out}, since the matter and mass fluctuations disappear. We present our results using the radius r_L^{out} and the mass contrast $\Delta_L \equiv \Delta(r_L, t_0)$.

Despite the fact that Eq. (19) can constrain the deviations from the FLRW model by constraining Δ_C and z_B, this prior does not constrain the cosmological parameters needed to assess the information contained in perturbations, for instance $P_{m,0}$. On the other hand, CMB observations should describe the early Universe at any point and, in particular, also at our observing position if the Copernican principle is valid. That is, under the assumption of the Copernican prior, CMB information such as the power spectrum should constrain Δ_C and z_B (and the background cosmological parameters).

We then compared the cosmological constraints on ΛLTB with the ones from the Copernican prior convolved with the CMB likelihood to obtain P, the probability distribution of Δ_C and z_B, given the initial conditions obtained from the CMB and their uncertainty, which, under the Copernican principle, describe matter perturbations around us:

$$P(\Delta_C, z_B) = \int dp_i \, \mathcal{P}(\Delta_C, z_B) \, \mathcal{L}_{CMB}(p_i, \Delta_C, z_B), \qquad (20)$$

where p_i denotes the standard ΛCDM parameters and $\mathcal{L}_{CMB}$ is the CMB likelihood of Sect. 3.2.

5. Results

As mentioned in Sect. 2.3, we explore the parameter space using the monteLLTB code: a cosmological solver and sampler for the ΛLTB model. Most of the plots shown in this Sect. have been produced using getdist (Lewis 2019).

Specifically, we constrained the ΛLTB model using several combinations of current and forecast data. We defined as a baseline analysis (hereafter 'Base') the combination of CMB, Pantheon SN, LSST, and H_0 data; however, we neglected possible correlations between LSST and Pantheon. We also defined the baseline analysis relative to current data (hereafter 'Base C') as the combination of CMB, Pantheon, and M_B data, with the last being the B-band absolute magnitude of SNe as inferred by the Cepheid distances (see Camarena et al. 2022). We neglected any possible correlation between the future DESI and *Euclid* dataset with the current BAOs. When DESI and *Euclid* data are combined, we replaced DESI measurements between $z \in [0.95, 1.75]$ with the *Euclid* data points.

Table 2. Ratios of the areas of the 95% contours from observations and the Copernican principle (see Fig. 2). We also include (last row) the case with background curvature, $K_B \neq 0$ in Eq. (10).

Observables	A_{obs}/A_{CP}	
	$0 \leq r_L^{out}$	$190\,\mathrm{Mpc} \leq r_L^{out}$
Flat background FLRW metric		
Base (CMB+Pantheon+LSST+H_0)	0.82	2.1
Base + BAO + *Euclid*	0.80	2.0
Base + BAO + DESI	0.78	1.9
Base + BAO + *Euclid* + DESI	0.75	1.9
Data above + *y*-dist. + kSZ	0.75	1.7
Curved background FLRW metric		
Data above	0.82	1.9

We now present separately our results for the cases of the ΛCDM and ΛLTB fiducial models of Table 1. As said earlier, we use the ΛCDM fiducial model to test how well future data can constrain deviations from the FLRW metric, while we use the ΛLTB fiducial models to see if future data can detect a violation of the Copernican principle.

5.1. ΛCDM mocks

5.1.1. The Copernican principle in light of the forthcoming surveys

In Fig. 2 we show the marginalised constraints at the 95% and 99% confidence levels on the integrated mass contrast, Δ_L, and the comoving size, r_L^{out}, for three different data combinations as compared to the constraints coming from the Copernican prior convolved with the CMB likelihoods.

The constraining power of future surveys on the radial inhomogeneity can be quantitatively compared to the expectation from the Copernican prior and CMB by comparing the ratio of the 95% confidence regions in the parameter space (see Table 2). Considering all scales, the ratio is always less than one, showing the capability of future surveys to rule out non-Copernican structures. However, at large scales, constraints provided by data still allow for non-Copernican mass density fluctuations since for $r_L^{out} \geq 190\,\mathrm{Mpc}$ the ratio is approximately equal to two. We note that, for both cases, the combination Base + DESI + *Euclid* provides constraints comparable to those obtained from the combination of all data, pointing out the important role that forthcoming LSS surveys will have to test the Copernican principle.
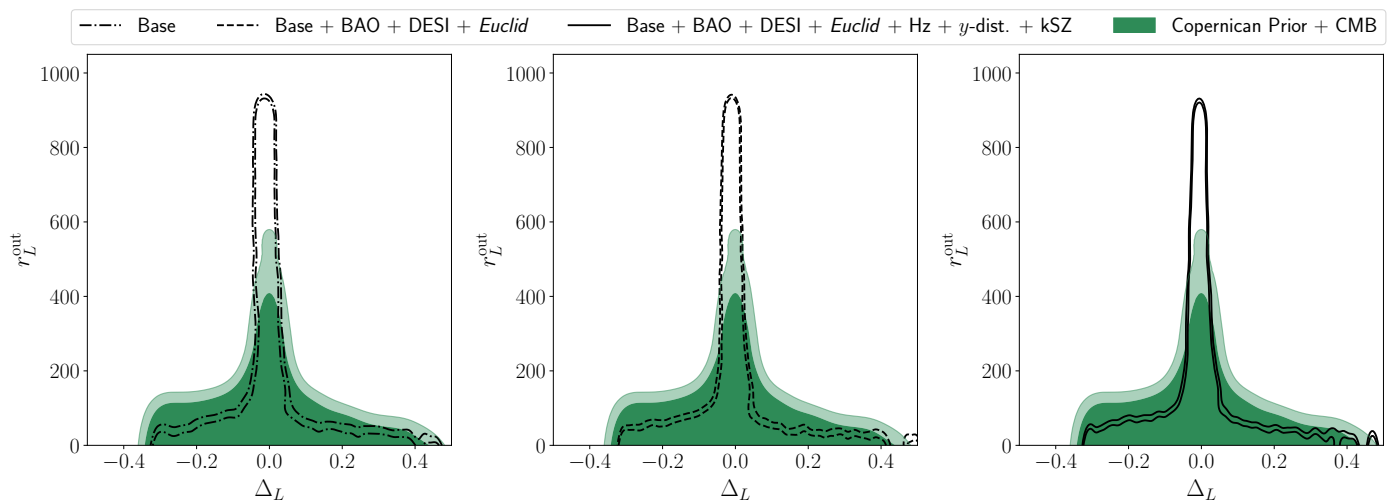
Fig. 2. 95% and 99% confidence level constraints on the integrated mass contrast, Δ_{L}, and the comoving size, $r_{\mathrm{L}}^{\mathrm{out}}$, for three different data combinations as compared to the constraints from the Copernican prior convolved with the CMB likelihoods.

Table 3. Percent improvement on constraints on radial inhomogeneity from next-generation surveys as compared to present-day constraints.

Observables considered in this analysis	Present-day observables considered in Camarena et al. (2021)	Percent improvement	
		$0 \le r_{\mathrm{L}}^{\mathrm{out}}$	$190\,\mathrm{Mpc} \le r_{\mathrm{L}}^{\mathrm{out}}$
Base	Base C (CMB + Pantheon + M_0)	29%	28%
	Base C + BAO + HZ	26%	28%
	Base C + BAO + HZ + y-dist. + kSZ	20%	0%
Base + BAO + *Euclid* + DESI	Base C	35%	34%
	Base C + BAO + HZ	32%	34%
	Base C + BAO + HZ + y-dist. + kSZ	26%	10%
Base + BAO + *Euclid* + DESI + y-dist. + kSZ	Base C	35%	41%
	Base C + BAO + HZ	32%	41%
	Base C + BAO + HZ + y-dist. + kSZ	26%	19%

We also consider the case of non-zero background curvature, that is, $K_{\mathrm{B}} \ne 0$ in Eq. (10). The result is shown in the last row of Table 2. The inclusion of background curvature degrades the constraints by approximately 10% compared to the flat case, still providing a competitive constraint on the non-Copernican parameters.

5.1.2. Comparison with present-day constraints

In order to quantify the role of future surveys in constraining inhomogeneity around us, we compare our constraints with the ones from current data only, as obtained in Camarena et al. (2021). Specifically, we compute the improvement on the observed area A_{obs} considering the data combinations presented in Table 3. Our present analyses do not include a cosmic chronometer dataset as contributions of this kind of data are expected to be secondary as compared with SNe and BAOs (Camarena et al. 2021). We note that our previous implementation of such data did not include the full covariance matrix presented in Moresco et al. (2020), revised and discussed in Moresco et al. (2022).

Our Base analysis shows an improvement upon the current constraints by more than 20%, when all scales are considered, and provides an improvement of 28% when compared to the constraints from Base C and Base C + BAO + HZ at scales $r_{\mathrm{L}}^{\mathrm{out}} \ge 190\,\mathrm{Mpc}$, where HZ denotes the cosmic chronometers dataset used in Camarena et al. (2021). It is interesting to note that our forecast Base analysis provides constraints comparable to those obtained with all the latest cosmological data available, Base C + BAO + HZ + y-dist + kSZ case, showing the importance of forthcoming SN surveys and 1% prior on the Hubble constant.

On the other hand, LSS surveys will play an important role in testing the Copernican principle. As shown in Table 3, future measurements from *Euclid* and DESI will sharpen the current constraints of Base C by approximately 35%, both at $0 \le r_{\mathrm{L}}^{\mathrm{out}}$ and $190\,\mathrm{Mpc} \le r_{\mathrm{L}}^{\mathrm{out}}$. The inclusion of *Euclid* and DESI will also tighten the parameter space by more than 30% compared to the combination Base C + BAO + HZ. When compared to the combination Base C + BAO + HZ + y-dist. + kSZ, our analysis with the forthcoming *Euclid* and DESI data shows an improvement of 26% for $0 \le r_{\mathrm{L}}^{\mathrm{out}}$ and 10% for $190\,\mathrm{Mpc} \le r_{\mathrm{L}}^{\mathrm{out}}$.

Finally, the combination of all data considered here will tighten our current constraints, leading to improvements up to 41% for scales at $190\,\mathrm{Mpc} \le r_{\mathrm{L}}^{\mathrm{out}}$ and 35% for $0 \le r_{\mathrm{L}}^{\mathrm{out}}$ (see Table 3).
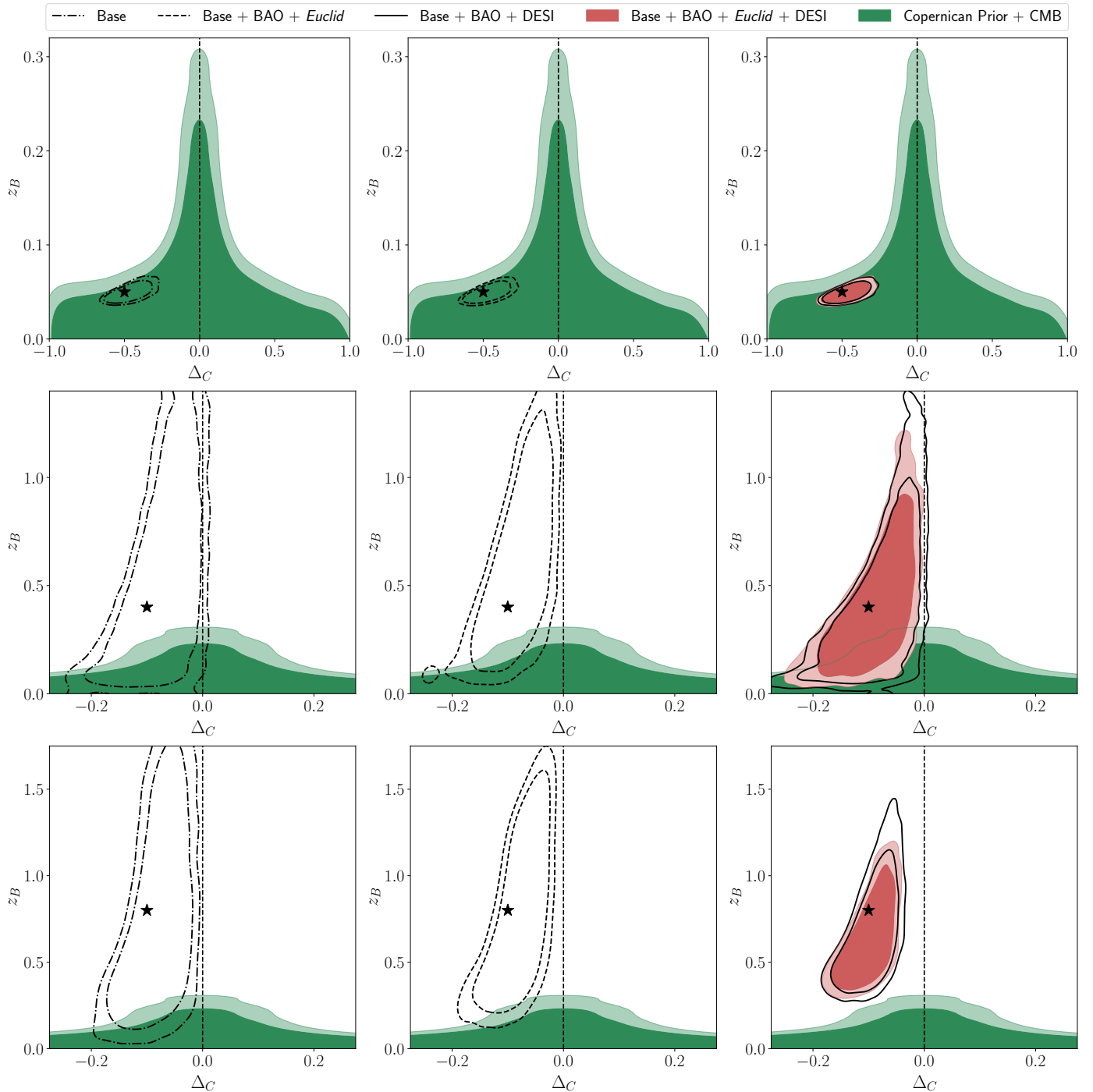
Fig. 3. 95% and 99% confidence level constraints on the contrast at the centre, Δ_C, and the redshift of the boundary, z_B, for the ΛLTB mock catalogues of Table 1 as compared to the constraints from the Copernican prior convolved with the CMB likelihood. The black star is placed at the fiducial values for the LTB parameters, i.e. $\Delta_C = -0.5$ and $z_B = 0.05$ (top row, ΛLTB 1), $\Delta_C = -0.1$ and $z_B = 0.4$ (middle row, ΛLTB 2), and $\Delta_C = -0.1$ and $z_B = 0.8$ (bottom row, ΛLTB 3). We note that the z_B axis is not same for all figures.

5.2. ΛLTB mocks

In Fig. 3 we show the marginalised constraints at the 95% and 99% confidence levels on Δ_C and z_B, for the three ΛLTB fiducial cosmologies, as compared to the constraints coming from the Copernican prior and CMB observations.

From the analysis relative to ΛLTB 1 (top row), we can see that future data will be able to probe the local structure. This means that the effect of the cosmic variance on the position of the observer will be reduced thanks to the forthcoming surveys.

On the other hand, from the analysis relative to ΛLTB 2 (middle row) and 3 (bottom row), we see that inhomogeneities that are large, but relatively shallow, can be detected with high significance thanks to future data. More precisely, one can note that our analyses exclude the FLRW case ($\Delta_C = 0$ and $z_B = 0$) by $\gtrsim 3\sigma$ (pink contours). This stresses the important roles of the next-generation surveys in testing the Copernican principle.

6. Discussion

6.1. The role of large-scale structure data

We have seen from the results of Sect. 5.1 on the ΛCDM mocks that future surveys, such as *Euclid*, will grant a ≈ 30% improvement on inhomogeneity around the observer. In particular, for scales greater than 190 Mpc, the combination of all data will constrain inhomogeneity to only 1.7 times the area of the region allowed by standard cosmology. Given the fact that *Euclid* probes the redshift range $0.9 < z < 1.8$, one may wonder if the improvement due to *Euclid* comes directly from better constraints on the shape of the angular diameter distance and Hubble rate or indirectly from better constraints on the cosmological parameters.

In order to answer the previous question we show in Fig. 4 the fluctuations in the apparent magnitude, Hubble rate and angular diameter distance for the ΛLTB model as compared to the fiducial ΛCDM one. The 68% and 95% bands are obtained by evaluating the relevant functions at every point of the chains. We compare three analyses: the Base one, Base with present BAO and *Euclid*, and Base with present BAOs and DESI. From this plot, it appears that the shape of the various functions does not change when adding *Euclid* or DESI. In other words, these two surveys do not improve the constraints in specific redshift ranges but rather they help at tightening the overall uncertainties. From this we conclude that the improvement due to *Euclid* comes mostly from better constraints on the cosmological parameters, although this works in synergy with DESI and the other observables.

6.2. Beyond the central observer

As mentioned earlier, our aim is to test radial homogeneity around us, neglecting anisotropies. We then placed the observer at the centre of the spherical over/underdensity. However, in an inhomogeneous universe beyond FLRW, neglecting anisotropies could not be justified because anisotropies may affect observables as much as radial inhomogeneities. In other words, the modelling adopted in this work implies a spherically symmetric inhomogeneity and a fine-tuning of the observer's position.

From the results of Sect. 5.1 on the ΛCDM mocks we see, a posteriori, that large structures with shallow contrasts are allowed by future data. If, for example, we consider a contrast of $\delta = -0.1$, the corresponding change in the Hubble rate is approximately $\delta H_0/H_0 = -f(\Omega_m)\delta/3 \simeq 0.017$, where $f \simeq 0.5$ is the present-day growth rate for the concordance ΛCDM model. The CMB dipole, if the observer were at, for example, a distance $d_{obs} = 300$ Mpc from the centre, using $v = \Delta H\, d_{obs}$, is then

$$\beta = \frac{v}{c} \simeq 1.2 \times 10^{-3}\,, \tag{21}$$

which is basically the observed CMB dipole (Aghanim et al. 2020a). As the structures that we consider in this work extend to, at most, 1000 Mpc (see Fig. 2), the required fine-tuning has a chance of less than 1 in 40. In other words, the fine-tuning required to satisfy the CMB dipole is rather mild and therefore the motivation for considering an off-centre observer is to provide a better description of possibly anisotropic data, rather than to relieve the fine-tuning of the observer's position.

It is worth mentioning that the fine-tuning is instead very severe when considering void models as alternatives to dark energy, a possibility that was not explored here and not favoured by data (see Marra et al. 2022). Indeed, in this case the underdensity has a radius of ≈ 3 Gpc and $\delta H_0/H_0 \approx 0.2$ so that the

observer has to be within ≈ 30 Mpc from the centre, giving rise to a fine-tuning of one in a million (Marra & Notari 2011). We note, however, as pointed out in Garcia-Bellido & Haugboelle (2008b), that it is possible to alleviate this improbability by displacing the observer and then making them move towards the centre. For distances of a few hundred Mpc and velocities of a few thousand km s^{-1}, the effect is indistinguishable from the observed CMB dipole. In a way, one exchanges an improbability in location for an improbability in the direction of motion. The overall effect is to reduce the coincidence to a few parts in a thousand.

7. Conclusions

Testing fundamental assumptions of cosmology is a crucial step towards improving our understanding of the Universe and firmly establishing the foundations of the standard cosmological paradigm. In this work we have tested the Copernican principle by placing constraints on the ΛLTB model using current and forecast data products. Specifically, we focused on the capability of *Euclid* to test the Copernican principle in conjunction with data from current and forthcoming surveys, such as SH0ES, DESI, and LSST.

In particular, we compared constraints on the ΛLTB model coming from the forecast and current data against constraints drawn from the Copernican prior—the statistical counterpart of the Copernican principle. This comparison allowed us to quantify how well we can constrain deviations from the Copernican principle.

We have considered two types of fiducial models: the standard ΛCDM model and the inhomogeneous ΛLTB model. By analysing the latter we aimed to determine if next-generation surveys will be able to detect deviations from the Copernican principle, while our analysis of ΛCDM data aimed to investigate if forthcoming data can successfully test the Copernican principle.

We have found that the inclusion of data from *Euclid*, and other future surveys, will improve the current constraints on the Copernican principle by up to 40%. This improvement will be especially important at scales $r_B \geq 190$ Mpc, where the inclusion of *Euclid*, and other forthcoming surveys, will reduce the constrained area of the space parameters by a factor of < 2 as compared with the area allowed by the Copernican prior. Furthermore, we find that using the forthcoming *Euclid* data, and data from other future surveys, we will be able to detect inhomogeneous deviations of the FLRW metric, including gigaparsec-scale inhomogeneities of contrast −0.1. Our analyses show that, given the precision of *Euclid* and other forthcoming surveys, a detection of this kind would allow us to rule out the FLRW space-time ($\Delta_C = 0$ and $z_B = 0$) by $\gtrsim 3\sigma$.

Our results rely on the assumption of a particular curvature profile, and, as shown in Appendix A, constraints could be weakened by up to a factor of ∼ 2 under the assumption of a more general profile. This drawback in our analysis, produced by the choice of a particular curvature profile, could be overcome by introducing data-driven methods that allow us to reconstruct the local distribution of matter in a more robust way. We will implement approaches of this sort in future research.

In summary, this work highlights the importance of synergies between *Euclid* and external probes in testing the Copernican principle, which is one of the fundamental assumptions of the standard cosmological paradigm.
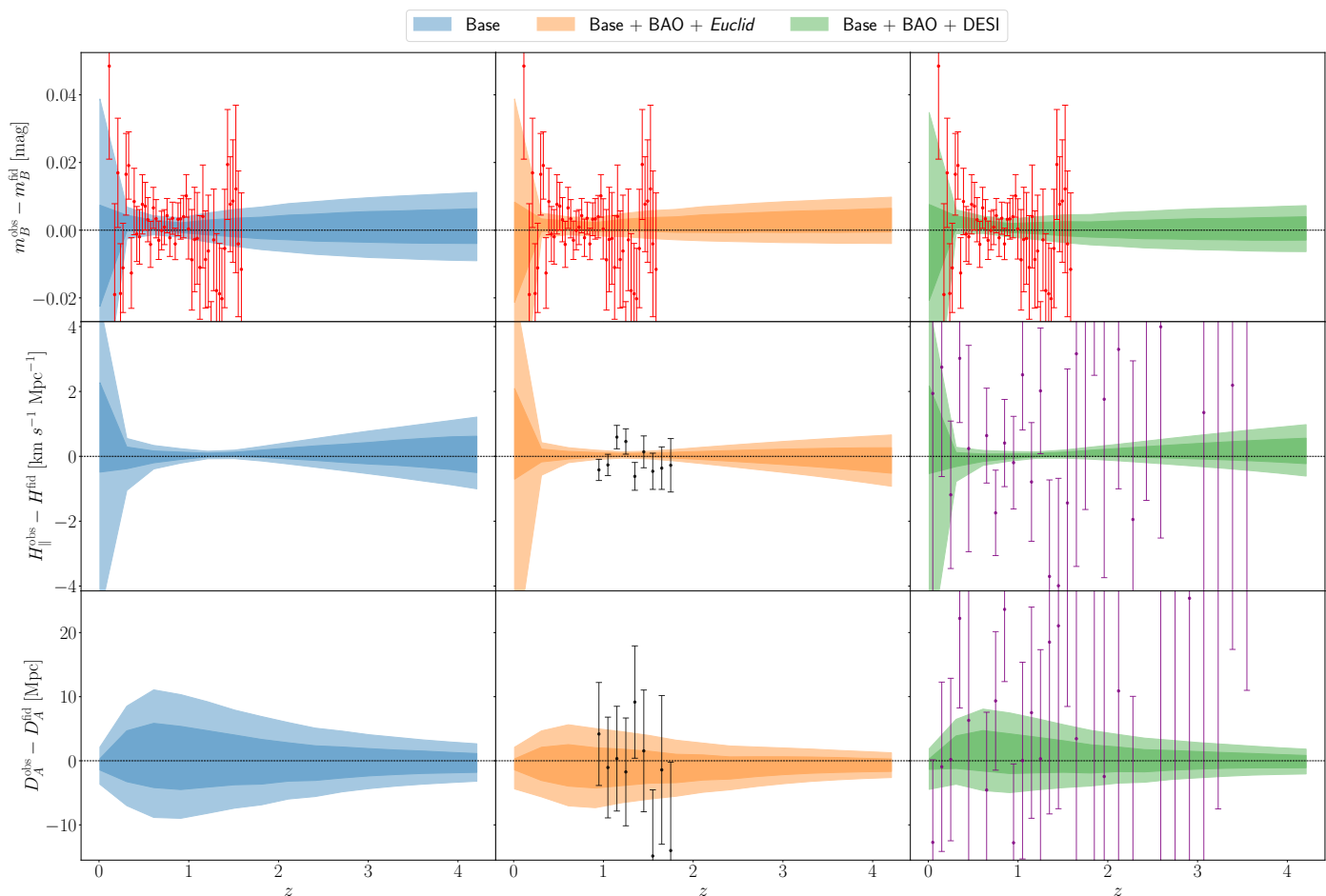
Fig. 4. Fluctuations in the apparent magnitude (top row), Hubble rate (middle row), and angular diameter distance (bottom row) for the ΛLTB model as compared to the fiducial ΛCDM one. The 68% and 95% bands are obtained by evaluating the relevant functions at every point of the chains. The red points show LSST and *Euclid* DESIRE SN data, the black ones *Euclid* data, and the purple ones DESI data. See Sect. 6.1.

References

Abell, P. A. et al. 2009, arXiv e-prints, arXiv:0912.0201

Aghamousa, A. et al. 2016, arXiv e-prints, arXiv:1611.00036

Aghanim, N. et al. 2014, A&A, 571, A27

Aghanim, N. et al. 2020a, A&A, 641, A1

Aghanim, N. et al. 2020b, A&A, 641, A6, [Erratum: A&A 652, C4 (2021)]

Akrami, Y. et al. 2020, A&A, 644, A100

Alam, S. et al. 2017, MNRAS, 470, 2617

Albrecht, A., Bernstein, G., Cahn, R., et al. 2006, arXiv e-prints, arXiv:astro-ph/0609591

Aluri, P. K. et al. 2022 [arXiv:2207.05765]

Amendola, L. et al. 2018, LRR, 21, 2

Astier, P. et al. 2014, A&A, 572, A80

Audren, B., Lesgourgues, J., Benabed, K., & Prunet, S. 2013, JCAP, 1302, 001

Ben-Dayan, I., Gasperini, M., Marozzi, G., Nugier, F., & Veneziano, G. 2013, JCAP, 06, 002

Bengaly, C. A. P., Maartens, R., & Santos, M. G. 2018, JCAP, 04, 031

Beutler, F., Blake, C., Colless, M., et al. 2011, MNRAS, 416, 3017

Blas, D., Lesgourgues, J., & Tram, T. 2011, JCAP, 07, 034

Brinckmann, T. & Lesgourgues, J. 2019, PDU, 24, 100260

Camarena, D., Marra, V., Sakr, Z., & Clarkson, C. 2021, MNRAS, 509, 1291

Camarena, D., Marra, V., Sakr, Z., & Clarkson, C. 2022, Class. Quant. Grav., 39, 184001

Carrick, J., Turnbull, S. J., Lavaux, G., & Hudson, M. J. 2015, MNRAS, 450, 317

Chen, L., Huang, Q.-G., & Wang, K. 2019, JCAP, 02, 028

Colin, J., Mohayaee, R., Rameez, M., & Sarkar, S. 2017, MNRAS, 471, 1045

Colin, J., Mohayaee, R., Sarkar, S., & Shafieloo, A. 2011, MNRAS, 414, 264

Cropper, M., Pottinger, S., Azzollini, R., et al. 2018, Proc. SPIE Int. Soc. Opt. Eng., 10698, 1069828

Dalang, C. & Bonvin, C. 2022, Mon. Not. Roy. Astron. Soc., 512, 3895

de la Torre, S. & Guzzo, L. 2012, MNRAS, 427, 327

du Mas des Bourboux, H. et al. 2020, ApJ, 901, 153

Efstathiou, G. 2021, MNRAS, 505, 3866

Euclid Collaboration, Scaramella, R., Amiaux, J., et al. 2022, A&A, 662, A112

Euclid Collaboration: Blanchard, A., Camera, S., Carbone, C., et al. 2020, A&A, 642, A191

Euclid Collaboration: Paykari, P., Kitching, T., Hoekstra, H., et al. 2020, A&A, 635, A139

February, S., Larena, J., Smith, M., & Clarkson, C. 2010, MNRAS, 405, 2231

Feindt, U. et al. 2013, A&A, 560, A90

Ferreira, P. d. S. & Quartin, M. 2021, PRL, 127, 101301

Ferreira, T. & Marra, V. 2022, Mon. Not. Roy. Astron. Soc., 513, 5438

Fixsen, D., Cheng, E., Gales, J., et al. 1996, ApJ, 473, 576

Font-Ribera, A., McDonald, P., Mostek, N., et al. 2014, JCAP, 05, 023

Friedrich, O. et al. 2021, MNRAS, 508, 3125

Garcia-Bellido, J. & Haugboelle, T. 2008a, JCAP, 04, 003

Garcia-Bellido, J. & Haugboelle, T. 2008b, JCAP, 09, 016

Gong, Y., Cooray, A., & Chen, X. 2010, ApJ, 709, 1420

Harnois-Deraps, J., Giblin, B., & Joachimi, B. 2019, A&A, 631, A160

Hudson, M. J., Smith, R. J., Lucey, J. R., & Branchini, E. 2004, MNRAS, 352, 61

Ishak, M., Peel, A., & Troxel, M. A. 2013, PRL, 111, 251302

Jonsson, J., Sullivan, M., Hook, I., et al. 2010, MNRAS, 405, 535

Kim, Y., Park, C.-G., Noh, H., & Hwang, J.-c. 2022, Astron. Astrophys., 660, A139

Kronborg, T. et al. 2010, A&A, 514, A44

Laureijs, R. et al. 2011, arXiv e-prints, arXiv:1110.3193

Lewis, A. 2019, arXiv e-prints, arXiv:1910.13970

Lyke, B. W. et al. 2020, ApJS, 250, 8

Maciaszek, T., Ealet, A., Jahnke, K., et al. 2016, in Society of Photo-Optical Instrumentation Engineers (SPIE) Conference Series, Vol. 9904, Space Telescopes and Instrumentation 2016: Optical, Infrared, and Millimeter Wave, ed. H. A. MacEwen, G. G. Fazio, M. Lystrup, N. Batalha, N. Siegler, & E. C. Tong, 99040T

Marra, V., Castro, T., Camarena, D., Borgani, S., & Ragagnin, A. 2022, Astron. Astrophys., 664, A179

Marra, V. & Notari, A. 2011, CQG, 28, 164004

Marra, V., Quartin, M., & Amendola, L. 2013, PRD, 88, 063004

Martinelli, M. et al. 2020, A&A, 644, A80

Martinelli, M. et al. 2021, A&A, 654, A148

Migkas, K., Pacaud, F., Schellenberger, G., et al. 2021, A&A, 649, A151

Migkas, K., Schellenberger, G., Reiprich, T. H., et al. 2020, A&A, 636, A15

Mohayaee, R., Rameez, M., & Sarkar, S. 2021, EPJ ST, 230, 2067

Moresco, M., Amati, L., Amendola, L., et al. 2022, arXiv e-prints, arXiv:2201.07241

Moresco, M., Jimenez, R., Verde, L., Cimatti, A., & Pozzetti, L. 2020, ApJ, 898, 82

Moss, A., Zibin, J. P., & Scott, D. 2011, PRD, 83, 103515

Nesseris, S. et al. 2022, Astron. Astrophys., 660, A67

Pozzetti, L., Hirata, C. M., Geach, J. E., et al. 2016, A&A, 590, A3

Prieto, E., Amiaux, J., Auguères, J.-L., et al. 2012, in Society of Photo-Optical Instrumentation Engineers (SPIE) Conference Series, Vol. 8442, Space Telescopes and Instrumentation 2012: Optical, Infrared, and Millimeter Wave, ed. M. C. Clampin, G. G. Fazio, H. A. MacEwen, & J. Oschmann, Jacobus M., 84420W

Quartin, M., Marra, V., & Amendola, L. 2014, PRD, 89, 023009

Rahman, W., Trotta, R., Boruah, S. S., Hudson, M. J., & van Dyk, D. A. 2022, Mon. Not. Roy. Astron. Soc., 514, 139

Raichoor, A. et al. 2020, MNRAS, 500, 3254

Redlich, M., Bolejko, K., Meyer, S., Lewis, G. F., & Bartelmann, M. 2014, A&A, 570, A63

Reichardt, C. L. et al. 2021, ApJ, 908, 199

Ross, A. J., Samushia, L., Howlett, C., et al. 2015, MNRAS, 449, 835

Ross, A. J. et al. 2020, MNRAS, 498, 2354

Saha, S., Shaikh, S., Mukherjee, S., Souradeep, T., & Wandelt, B. D. 2021, JCAP, 10, 072

Scolnic, D. et al. 2018, ApJ, 859, 101

Secrest, N. J., von Hausegger, S., Rameez, M., et al. 2021, ApJL, 908, L51

Siewert, T. M., Schmidt-Rubart, M., & Schwarz, D. J. 2021, A&A, 653, A9

Silk, J. 1977, A&A, 59, 53

Valkenburg, W. 2012, GRG, 44, 2449

Valkenburg, W., Marra, V., & Clarkson, C. 2014, MNRAS, 438, L6

Wang, Y., Chuang, C.-H., & Hirata, C. M. 2013, MNRAS, 430, 2446

Yadav, J. K., Bagla, J. S., & Khandai, N. 2010, Mon. Not. Roy. Astron. Soc., 405, 2009

Zibin, J. P. 2008, PRD, 78, 043504

[1] PPGCosmo, Universidade Federal do Espírito Santo, 29075-910,Vitória, ES, Brazil

[2] Núcleo Cosmo-ufes & Departamento de Física, Universidade Federal do Espírito Santo, 29075-910, Vitória, ES, Brazil

[3] INAF-Osservatorio Astronomico di Trieste, Via G. B. Tiepolo 11, I-34143 Trieste, Italy

[4] IFPU, Institute for Fundamental Physics of the Universe, via Beirut 2, 34151 Trieste, Italy

[5] Institut de Recherche en Astrophysique et Planétologie (IRAP), Université de Toulouse, CNRS, UPS, CNES, 14 Av. Edouard Belin, F-31400 Toulouse, France

[6] Institut für Theoretische Physik, University of Heidelberg, Philosophenweg 16, 69120 Heidelberg, Germany

[7] Université St Joseph; Faculty of Sciences, Beirut, Lebanon

[8] Instituto de Física Teórica UAM-CSIC, Campus de Cantoblanco, E-28049 Madrid, Spain

[9] Departamento de Física, Faculdade de Ciências, Universidade de Lisboa, Edifício C8, Campo Grande, PT1749-016 Lisboa, Portugal

[10] Instituto de Astrofísica e Ciências do Espaço, Faculdade de Ciências, Universidade de Lisboa, Campo Grande, PT-1749-016 Lisboa, Portugal

[11] Institut de Physique Théorique, CEA, CNRS, Université Paris-Saclay F-91191 Gif-sur-Yvette Cedex, France

[12] Université de Genève, Département de Physique Théorique and Centre for Astroparticle Physics, 24 quai Ernest-Ansermet, CH-1211 Genève 4, Switzerland

[13] INAF-Osservatorio Astronomico di Roma, Via Frascati 33, I-00078 Monteporzio Catone, Italy

[14] Centro de Astrofísica da Universidade do Porto, Rua das Estrelas, 4150-762 Porto, Portugal

[15] Instituto de Astrofísica e Ciências do Espaço, Universidade do Porto, CAUP, Rua das Estrelas, PT4150-762 Porto, Portugal

[16] Departamento de Física, FCFM, Universidad de Chile, Blanco Encalada 2008, Santiago, Chile

[17] School of Physics and Astronomy, Queen Mary University of London, Mile End Road, London E1 4NS, UK

[18] Dipartimento di Fisica, Universitá degli Studi di Torino, Via P. Giuria 1, I-10125 Torino, Italy

[19] INFN-Sezione di Torino, Via P. Giuria 1, I-10125 Torino, Italy

[20] INAF-Osservatorio Astrofisico di Torino, Via Osservatorio 20, I-10025 Pino Torinese (TO), Italy

[21] INAF-IASF Milano, Via Alfonso Corti 12, I-20133 Milano, Italy

[22] Institute for Theoretical Particle Physics and Cosmology (TTK), RWTH Aachen University, D-52056 Aachen, Germany

[23] Université Paris-Saclay, CNRS/IN2P3, IJCLab, 91405 Orsay, France

[24] Centre National d'Etudes Spatiales, Toulouse, France

[25] Université Paris-Saclay, Université Paris Cité, CEA, CNRS, Astrophysique, Instrumentation et Modélisation Paris-Saclay, 91191 Gif-sur-Yvette, France

[26] Institute of Space Sciences (ICE, CSIC), Campus UAB, Carrer de Can Magrans, s/n, 08193 Barcelona, Spain

[27] Institut d'Estudis Espacials de Catalunya (IEEC), Carrer Gran Capitá 2-4, 08034 Barcelona, Spain

[28] Université Paris-Saclay, CNRS, Institut d'astrophysique spatiale, 91405, Orsay, France

[29] ESAC/ESA, Camino Bajo del Castillo, s/n., Urb. Villafranca del Castillo, 28692 Villanueva de la Cañada, Madrid, Spain

[30] Institute of Cosmology and Gravitation, University of Portsmouth, Portsmouth PO1 3FX, UK

[31] INAF-Osservatorio di Astrofisica e Scienza dello Spazio di Bologna, Via Piero Gobetti 93/3, I-40129 Bologna, Italy

[32] Dipartimento di Fisica e Astronomia "Augusto Righi" - Alma Mater Studiorum Università di Bologna, via Piero Gobetti 93/2, I-40129 Bologna, Italy

[33] INFN-Sezione di Bologna, Viale Berti Pichat 6/2, I-40127 Bologna, Italy

[34] Dipartimento di Fisica, Universitá degli studi di Genova, and INFN-Sezione di Genova, via Dodecaneso 33, I-16146, Genova, Italy

[35] INFN-Sezione di Roma Tre, Via della Vasca Navale 84, I-00146, Roma, Italy

[36] INAF-Osservatorio Astronomico di Capodimonte, Via Moiariello 16, I-80131 Napoli, Italy

[37] Mullard Space Science Laboratory, University College London, Holmbury St Mary, Dorking, Surrey RH5 6NT, UK

[38] Institut de Física d'Altes Energies (IFAE), The Barcelona Institute of Science and Technology, Campus UAB, 08193 Bellaterra (Barcelona), Spain

[39] Port d'Informació Científica, Campus UAB, C. Albareda s/n, 08193 Bellaterra (Barcelona), Spain

[40] INFN section of Naples, Via Cinthia 6, I-80126, Napoli, Italy

[41] Department of Physics "E. Pancini", University Federico II, Via Cinthia 6, I-80126, Napoli, Italy

[42] Dipartimento di Fisica e Astronomia "Augusto Righi" - Alma Mater Studiorum Universitá di Bologna, Viale Berti Pichat 6/2, I-40127 Bologna, Italy

[43] INAF-Osservatorio Astrofisico di Arcetri, Largo E. Fermi 5, I-50125, Firenze, Italy

[44] Institut national de physique nucléaire et de physique des particules, 3 rue Michel-Ange, 75794 Paris Cédex 16, France

[45] Institute for Astronomy, University of Edinburgh, Royal Observatory, Blackford Hill, Edinburgh EH9 3HJ, UK

[46] European Space Agency/ESRIN, Largo Galileo Galilei 1, 00044 Frascati, Roma, Italy

[47] Univ Lyon, Univ Claude Bernard Lyon 1, CNRS/IN2P3, IP2I Lyon, UMR 5822, F-69622, Villeurbanne, France

[48] Observatoire de Sauverny, Ecole Polytechnique Fédérale de Lausanne, CH-1290 Versoix, Switzerland

[49] Department of Astronomy, University of Geneva, ch. dÉcogia 16, CH-1290 Versoix, Switzerland

[50] Department of Physics, Oxford University, Keble Road, Oxford OX1 3RH, UK

[51] Jodrell Bank Centre for Astrophysics, Department of Physics and Astronomy, University of Manchester, Oxford Road, Manchester M13 9PL, UK

[52] INFN-Padova, Via Marzolo 8, I-35131 Padova, Italy

[53] Istituto Nazionale di Astrofisica (INAF) - Osservatorio di Astrofisica e Scienza dello Spazio (OAS), Via Gobetti 93/3, I-40127 Bologna, Italy

[54] Istituto Nazionale di Fisica Nucleare, Sezione di Bologna, Via Irnerio 46, I-40126 Bologna, Italy

[55] INAF-Osservatorio Astronomico di Padova, Via dell'Osservatorio 5, I-35122 Padova, Italy

[56] Max Planck Institute for Extraterrestrial Physics, Giessenbachstr. 1, D-85748 Garching, Germany

[57] Universitäts-Sternwarte München, Fakultät für Physik, Ludwig-Maximilians-Universität München, Scheinerstrasse 1, 81679 München, Germany

[58] Institute of Theoretical Astrophysics, University of Oslo, P.O. Box 1029 Blindern, N-0315 Oslo, Norway

[59] Jet Propulsion Laboratory, California Institute of Technology, 4800 Oak Grove Drive, Pasadena, CA, 91109, USA

[60] von Hoerner & Sulger GmbH, Schloßplatz 8, D-68723 Schwetzingen, Germany

[61] Technical University of Denmark, Elektrovej 327, 2800 Kgs. Lyngby, Denmark

[62] Max-Planck-Institut für Astronomie, Königstuhl 17, D-69117 Heidelberg, Germany

[63] Department of Physics and Helsinki Institute of Physics, Gustaf Hällströmin katu 2, 00014 University of Helsinki, Finland

[64] NOVA optical infrared instrumentation group at ASTRON, Oude Hoogeveensedijk 4, 7991PD, Dwingeloo, The Netherlands

[65] Argelander-Institut für Astronomie, Universität Bonn, Auf dem Hügel 71, 53121 Bonn, Germany

[66] Department of Physics, Institute for Computational Cosmology, Durham University, South Road, DH1 3LE, UK

[67] INFN-Bologna, Via Irnerio 46, I-40126 Bologna, Italy

[68] Institute of Physics, Laboratory of Astrophysics, Ecole Polytechnique Fédérale de Lausanne (EPFL), Observatoire de Sauverny, 1290 Versoix, Switzerland

[69] European Space Agency/ESTEC, Keplerlaan 1, 2201 AZ Noordwijk, The Netherlands

[70] Department of Physics and Astronomy, University of Aarhus, Ny Munkegade 120, DK-8000 Aarhus C, Denmark

[71] Space Science Data Center, Italian Space Agency, via del Politecnico snc, 00133 Roma, Italy

[72] Institute of Space Science, Bucharest, Ro-077125, Romania

[73] Instituto de Astrofísica de Canarias, Calle Vía Láctea s/n, E-38204, San Cristóbal de La Laguna, Tenerife, Spain

[74] Departamento de Astrofísica, Universidad de La Laguna, E-38206, La Laguna, Tenerife, Spain

[75] Aix-Marseille Univ, CNRS/IN2P3, CPPM, Marseille, France

[76] Dipartimento di Fisica e Astronomia "G.Galilei", Universitá di Padova, Via Marzolo 8, I-35131 Padova, Italy

[77] Aix-Marseille Univ, CNRS, CNES, LAM, Marseille, France

[78] Centro de Investigaciones Energéticas, Medioambientales y Tecnológicas (CIEMAT), Avenida Complutense 40, 28040 Madrid, Spain

[79] Instituto de Astrofísica e Ciências do Espaço, Faculdade de Ciências, Universidade de Lisboa, Tapada da Ajuda, PT-1349-018 Lisboa, Portugal

[80] Universidad Politécnica de Cartagena, Departamento de Electrónica y Tecnología de Computadoras, 30202 Cartagena, Spain

[81] Kapteyn Astronomical Institute, University of Groningen, PO Box 800, 9700 AV Groningen, The Netherlands

[82] Infrared Processing and Analysis Center, California Institute of Technology, Pasadena, CA 91125, USA

[83] INAF-Osservatorio Astronomico di Brera, Via Brera 28, I-20122 Milano, Italy

[84] Institut d'Astrophysique de Paris, UMR 7095, CNRS, and Sorbonne Université, 98 bis boulevard Arago, 75014 Paris, France

[85] Junia, EPA department, F 59000 Lille, France

Appendix A: The curvature profile

The analyses presented in this paper rely on the assumption of the compensated profile introduced in Sect. 2.2, which was chosen in order to ensure that the ΛCDM background is recovered at $r \geq r_B$, a crucial feature in order to confront CMB data consistently using an effective FLRW model.
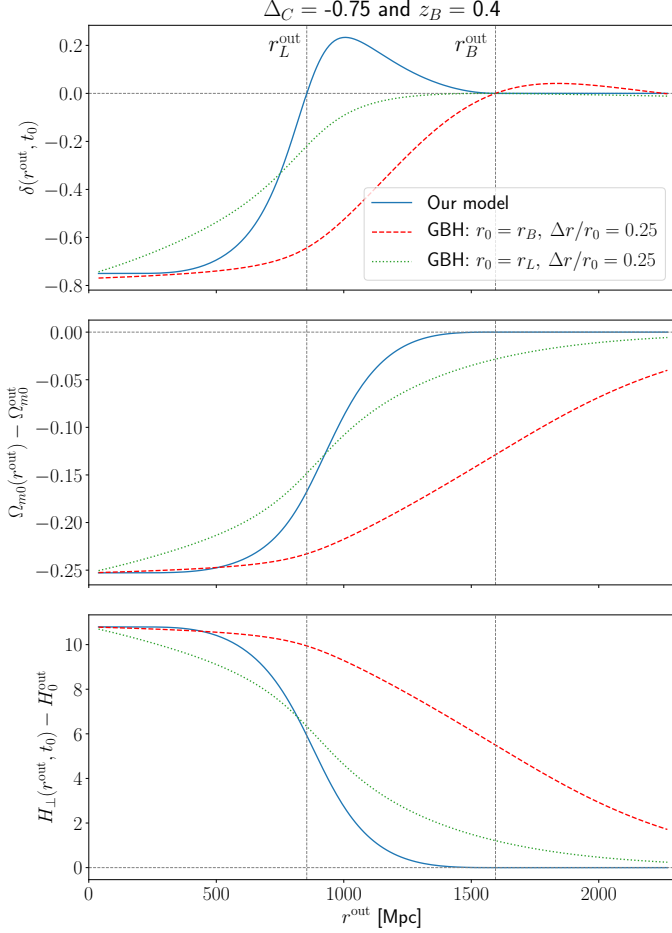

Fig. A.1. Comparison between our model and the GBH parametrization. Top: Density contrast of matter today, $\delta(r, t_0)$, as a function of the FLRW comoving coordinate. Our compensated model (solid blue line) satisfies $\delta(r_L^{out}, t_0) = \delta(r_B^{out}, t_0) = 0$, while the ΛCDM background is not exactly recovered for the GBH models (dashed red and dotted green lines). Middle: Deviations from the background density of matter, $\Omega_{m,0}^{out}$, as a function of the FLRW comoving coordinate. The GBH model with $r_0 = r_B$ (red dashed line) largely deviates from $\Omega_{m,0}^{out}$ at $r^{out} = r_B^{out}$. On the other hand, the choice of $r_0 = r_L$ for the GBH leads to deviations of approximately -0.01 from the background at $r^{out} = r_B^{out}$. The model assumed in this work fully recovers $\Omega_{m,0}^{out}$ at any $r^{out} \geq r_B^{out}$. Bottom: Deviations from the background Hubble expansion as a function of the FLRW comoving coordinate. GBH models (dashed red and dotted green lines) do not perfectly match the ΛCDM background expansion history at $r^{out} = r_B^{out}$.

Here, we compare our model to the Garcia-Bellido and Haugboelle (GBH) model (Garcia-Bellido & Haugboelle 2008a), which parametrises the LTB metric by imposing

$$\Omega_{m,0}(r) = \Omega_{m,0}^{out} + \left(\Omega_{m,0}^{in} - \Omega_{m,0}^{out}\right) \left\{ \frac{1 - \tanh\left[(r - r_0)/2\Delta r\right]}{1 + \tanh\left[r_0/2\Delta r\right]} \right\},$$

$$H_0(r) = H_{\perp 0}^{out} + \left(H_{\perp 0}^{in} - H_{\perp 0}^{out}\right) \left\{ \frac{1 - \tanh\left[(r - r_0)/2\Delta r\right]}{1 + \tanh\left[r_0/2\Delta r\right]} \right\},$$

where r_0 is the size of the void, Δr the transition scale, $\Omega_{m,0}^{in} \equiv \Omega_{m,0}(r = 0)$, and $H_{\perp 0}^{in} \equiv H_{\perp 0}(r = 0)$. Fig. A.1 shows the differences between our model (solid blue line) and the GBH model, where we have adopted $r_0 = r_L$ (dotted green line) and $r_0 = r_B$ (dashed red line). When the size of the GBH inhomogeneity is fixed to r_B, a scale greater that r_B is needed to recover the ΛCDM background. On the other hand, if one assumes $r_0 = r_L$, the GBH model tends to the ΛCDM background at $r = r_B$. In contrast, our model perfectly matches the ΛCDM background at any scale $r \geq r_B$. The compensating behaviour of our model is particularly notable in the top panel of the Fig. A.1, where we note that $\delta(r_L^{out}, t_0) = \delta(r_B^{out}, t_0) = 0$ for our model while the GBH models does not satisfy $\delta(r^{out}, t_0) = 0$ for all $r^{out} \geq r_B^{out}$.

Furthermore, to investigate the dependence of our results on the chosen profile, we performed an additional analysis using the following generalisation of Eq. (10):

$$P_3(x, \alpha) = \begin{cases} 1 & \text{for } 0 \leq x < \alpha \\ 1 - \exp\left[-\frac{1-\alpha}{x-\alpha}\left(1 - \frac{x-\alpha}{1-\alpha}\right)^3\right] & \text{for } \alpha \leq x < 1 \\ 0 & \text{for } 1 \leq x \end{cases}, \quad \text{(A.1)}$$

with $0 < \alpha < 1$. This new parameter will modify the smoothness of the transition between the inner and compensating region, leading to sharpened profiles when α approximates to 1. Results from this extra analysis, which is performed using the combination Base + BAO + *Euclid* + DESI + *y*-dist. + kSZ from the ΛCDM fiducial, shows that the inclusion of the α parameter weakens the constraints on Δ_C and r_L^{out} by a factor of two, compared to the results from Eq. (10).

Appendix B: Re-scaling datasets

Covariance matrices are fundamental pieces of forecast analyses. However, their production for forthcoming surveys is an open issue when non-standard cosmologies are considered (Harnois-Deraps et al. 2019; Friedrich et al. 2021; Ferreira & Marra 2022). This complicates the construction of forecast data for ΛLTB cosmologies. Nesseris et al. (2022) has overcome this issue by neglecting the error due to the non-standard cosmology. Here, we apply a re-scaling method to convert the ΛCDM forecast data and its covariance matrices into ΛLTB catalogues.

Consider a given dataset, with x_i being the observed quantity, z_i the corresponding redshift, and C_{ij} the covariance matrix. This dataset can be re-scaled to agree with a particular model via the following steps.

First, we define $R_{ij} = C_{ij}/x_i x_j$, a new matrix that contains the relative uncertainties and correlations from the original covariance matrix. Second, we compute with the theoretical prediction of the new model the fiducial values at the relevant redshifts, such that $x_i^f \equiv x^{fid}(z_i)$. Third, using the above defined quantities, we compute the new correlation matrix as $\tilde{C}_{ij} = x_i^f x_j^f R_{ij}$. Finally, we then draw a random realisation, $\tilde{x}_i$, of the multivariate-normal distribution $\mathcal{N}(x_i^f, \tilde{C}_{ij})$.

We note that this method assumes that relative error and correlations are not changed by a non-standard model. As discussed through this paper, the procedure above is also applied to re-scale real data according the fiducial models presented on Table 1; this ensures that all data are consistently described by a particular fiducial model.

Appendix C: The inhomogeneous Hubble constant

The ΛLTB model features a profile function $H_0(r)$ that depends on the radial distance from the centre of the void, instead of a

constant value like H_0 in the ΛCDM model. Since there is not a preferable scale to set the rate of expansion of the Universe, the definition of H_0 remains arbitrary. To overcome this issue, we extend the FLRW definitions and mimic the observational procedure to locally constrain the Hubble constant. Explicitly, we adopt the definition $H_0^{\rm L}$ for inhomogeneous cosmological models that was introduced in Camarena et al. (2022). This method, which is applied for every sample point of the parameter space, follows the following steps.

First, we create a mock catalogue using the redshifts of Pantheon SNe at $0.023 < z < 0.15$ and the ΛLTB luminosity distances at the corresponding redshifts. Second, the mock data are fitted using an extension of the cosmographic expansion given by

$$D_L(z) = \frac{cz}{H_0^{\rm L}} \left[1 + \frac{(1 - q_0^r)z}{2} \right], \tag{C.1}$$

$$q_0^r(r) = \left[\frac{\Omega_{\rm m}(r)}{2} - \Omega_\Lambda(r) \right] \left[\frac{H_0(r)}{H_0^{\rm L}} \right]^2, \tag{C.2}$$

where q_0^r is the radial-dependent deceleration parameter. Finally, the best-fit value of $H_0^{\rm L}$ is adopted as the measured Hubble constant.

It is interesting to point out that this procedure mimics the standard cosmic distance ladder analysis of SNe that follow the Hubble flow, while taking into account the effect of the inhomogeneity on the measurement of the Hubble constant. We note that other authors have previously proposed similar approximations (Redlich et al. 2014; Efstathiou 2021).